

1-28-2013

Scanning in Situ Spectroscopy Platform for Imaging Surgical Breast Tissue Specimens

Venkataramanan Krishnaswamy
Dartmouth College


Ashley M. Laughney
Dartmouth College

Wendy A. Wells
Dartmouth College

Keith D. Paulsen
Dartmouth College

Brian W. Pogue
Dartmouth College

Follow this and additional works at: <https://digitalcommons.dartmouth.edu/facoa>

 Part of the [Analytical, Diagnostic and Therapeutic Techniques and Equipment Commons](#),
[Bioimaging and Biomedical Optics Commons](#), and the [Neoplasms Commons](#)

Recommended Citation

Krishnaswamy, Venkataramanan; Laughney, Ashley M.; Wells, Wendy A.; Paulsen, Keith D.; and Pogue, Brian W., "Scanning in Situ Spectroscopy Platform for Imaging Surgical Breast Tissue Specimens" (2013). *Open Dartmouth: Faculty Open Access Articles*. 1575.
<https://digitalcommons.dartmouth.edu/facoa/1575>

This Article is brought to you for free and open access by Dartmouth Digital Commons. It has been accepted for inclusion in Open Dartmouth: Faculty Open Access Articles by an authorized administrator of Dartmouth Digital Commons. For more information, please contact dartmouthdigitalcommons@groups.dartmouth.edu.

Scanning *in situ* Spectroscopy platform for imaging surgical breast tissue specimens

Venkataramanan Krishnaswamy,^{1,*} Ashley M. Laughney,¹ Wendy A. Wells,² Keith D. Paulsen,¹ and Brian W. Pogue^{1,3}

¹Thayer School of Engineering, Dartmouth College, 14 Engineering Drive, Hanover, New Hampshire 03755, USA

²Department of Pathology, Geisel School of Medicine at Dartmouth, Hanover, New Hampshire 03755, USA

³brian.w.pogue@dartmouth.edu

*venkat.krishnaswamy@dartmouth.edu

Abstract: A non-contact localized spectroscopic imaging platform has been developed and optimized to scan 1x1cm² square regions of surgically resected breast tissue specimens with ~150-micron resolution. A color corrected, image-space telecentric scanning design maintained a consistent sampling geometry and uniform spot size across the entire imaging field. Theoretical modeling in ZEMAX allowed estimation of the spot size, which is equal at both the center and extreme positions of the field with ~5% variation across the designed waveband, indicating excellent color correction. The spot sizes at the center and an extreme field position were also measured experimentally using the standard knife-edge technique and were found to be within ~8% of the theoretical predictions. Highly localized sampling offered inherent insensitivity to variations in background absorption allowing direct imaging of local scattering parameters, which was validated using a matrix of varying concentrations of Intralipid and blood in phantoms. Four representative, pathologically distinct lumpectomy tissue specimens were imaged, capturing natural variations in tissue scattering response within a given pathology. Variations as high as 60% were observed in the average reflectance and relative scattering power images, which must be taken into account for robust classification performance. Despite this variation, the preliminary data indicates discernible scatter power contrast between the benign vs malignant groups, but reliable discrimination of pathologies within these groups would require investigation into additional contrast mechanisms.

©2013 Optical Society of America

OCIS codes: (170.3890) Medical optics instrumentation; (170.6510) Spectroscopy, tissue diagnostics; (290.5820) Scattering measurements.

References and links

1. V. Krishnaswamy, P. J. Hoopes, K. S. Samkoe, J. A. O'Hara, T. Hasan, and B. W. Pogue, "Quantitative imaging of scattering changes associated with epithelial proliferation, necrosis, and fibrosis in tumors using microsampling reflectance spectroscopy," *J. Biomed. Opt.* **14**(1), 014004 (2009).
2. B. W. Pogue and G. C. Burke, "Fiber-optic bundle design for quantitative fluorescence measurement from tissue," *Appl. Opt.* **37**(31), 7429–7436 (1998).
3. A. Myakov, L. Nieman, L. Wicky, U. Utzinger, R. Richards-Kortum, and K. Sokolov, "Fiber optic probe for polarized reflectance spectroscopy in vivo: Design and performance," *J. Biomed. Opt.* **7**(3), 388–397 (2002).
4. N. Subhash, J. R. Mallia, S. S. Thomas, A. Mathews, P. Sebastian, and J. Madhavan, "Oral cancer detection using diffuse reflectance spectral ratio R540/R575 of oxygenated hemoglobin bands," *J. Biomed. Opt.* **11**(1), 014018 (2006).
5. J.-G. Wu, Y.-Z. Xu, C.-W. Sun, R. D. Soloway, D.-F. Xu, Q.-G. Wu, K.-H. Sun, S.-F. Weng, and G.-X. Xu, "Distinguishing malignant from normal oral tissues using FTIR fiber-optic techniques," *Biopolymers* **62**(4), 185–192 (2001).
6. J. R. Mourant, I. J. Bigio, J. Boyer, R. L. Conn, T. Johnson, and T. Shimada, "Spectroscopic diagnosis of bladder cancer with elastic light scattering," *Lasers Surg. Med.* **17**(4), 350–357 (1995).
7. M. R. Austwick, B. Clark, C. A. Mosse, K. Johnson, D. W. Chicken, S. K. Somasundaram, K. W. Calabro, Y. Zhu, M. Falzon, G. Kocjan, T. Fearn, S. G. Bown, I. J. Bigio, and M. R. S. Keshtgar, "Scanning elastic scattering spectroscopy detects metastatic breast cancer in sentinel lymph nodes," *J. Biomed. Opt.* **15**(4), 047001 (2010).

8. J. Q. Brown, T. M. Bydlon, L. M. Richards, Bing Yu, S. A. Kennedy, J. Geradts, L. G. Wilke, M. K. Junker, J. Gallagher, W. T. Barry, and N. Ramanujam, "Optical Assessment of Tumor Resection Margins in the Breast," *IEEE J. Sel. Top. Quantum Electron.* **16**(3), 530–544 (2010).
9. S. Kennedy, J. Geradts, T. Bydlon, J. Q. Brown, J. Gallagher, M. Junker, W. Barry, N. Ramanujam, and L. Wilke, "Optical breast cancer margin assessment: an observational study of the effects of tissue heterogeneity on optical contrast," *Breast Cancer Res.* **12**(6), R91 (2010).
10. L. G. Wilke, J. Q. Brown, T. M. Bydlon, S. A. Kennedy, L. M. Richards, M. K. Junker, J. Gallagher, W. T. Barry, J. Geradts, and N. Ramanujam, "Rapid noninvasive optical imaging of tissue composition in breast tumor margins," *Am. J. Surg.* **198**(4), 566–574 (2009).
11. N. Lue, J. W. Kang, C.-C. Yu, I. Barman, N. C. Dingari, M. S. Feld, R. R. Dasari, and M. Fitzmaurice, "Portable optical fiber probe-based spectroscopic scanner for rapid cancer diagnosis: a new tool for intraoperative margin assessment," *PLoS ONE* **7**(1), e30887 (2012).
12. A. L. Clark, A. M. Gillenwater, T. G. Collier, R. Alizadeh-Naderi, A. K. El-Naggar, and R. R. Richards-Kortum, "Confocal microscopy for real-time detection of oral cavity neoplasia," *Clin. Cancer Res.* **9**(13), 4714–4721 (2003).
13. Y. Wang, M. Raj, H. S. McGuff, G. Bhawe, B. Yang, T. Shen, and X. Zhang, "Portable oral cancer detection using a miniature confocal imaging probe with a large field of view," *J. Micromech. Microeng.* **22**(6), 065001 (2012).
14. I. Itzkan, L. Qiu, H. Fang, M. M. Zaman, E. Vitkin, I. C. Ghiran, S. Salahuddin, M. Modell, C. Andersson, L. M. Kimerer, P. B. Cipolloni, K.-H. Lim, S. D. Freedman, I. Bigio, B. P. Sachs, E. B. Hanlon, and L. T. Perelman, "Confocal light absorption and scattering spectroscopic microscopy monitors organelles in live cells with no exogenous labels," *Proc. Natl. Acad. Sci. U.S.A.* **104**(44), 17255–17260 (2007).
15. D. S. Gareau, Y. Li, B. Huang, Z. Eastman, K. S. Nehal, and M. Rajadhyaksha, "Confocal mosaicing microscopy in Mohs skin excisions: feasibility of rapid surgical pathology," *J. Biomed. Opt.* **13**(5), 054001 (2008).
16. J. Bini, J. Spain, K. Nehal, V. Hazelwood, C. DiMarzio, and M. Rajadhyaksha, "Confocal mosaicing microscopy of human skin ex vivo: spectral analysis for digital staining to simulate histology-like appearance," *J. Biomed. Opt.* **16**(7), 076008 (2011).
17. W. F. Cheong, S. A. Prah, and A. J. Welch, "A review of the optical properties of biological tissues," *IEEE J. Quantum Electron.* **26**(12), 2166–2185 (1990).
18. V. Krishnaswamy, A. M. Laughney, K. D. Paulsen, and B. W. Pogue, "Dark-field scanning in situ spectroscopy platform for broadband imaging of resected tissue," *Opt. Lett.* **36**(10), 1911–1913 (2011).
19. J. A. Arnaud, W. M. Hubbard, G. D. Mandeville, B. de la Clavière, E. A. Franke, and J. M. Franke, "Technique for fast measurement of gaussian laser beam parameters," *Appl. Opt.* **10**(12), 2775–2776 (1971).
20. S. Srinivasan, B. W. Pogue, S. Jiang, H. Dehghani, C. Kogel, S. Soho, J. J. Gibson, T. D. Tosteson, S. P. Poplack, and K. D. Paulsen, "Interpreting hemoglobin and water concentration, oxygen saturation, and scattering measured in vivo by near-infrared breast tomography," *Proc. Natl. Acad. Sci. U.S.A.* **100**(21), 12349–12354 (2003).
21. Labsphere Inc, "Spectralon optical grade reflectance material," <http://labsphere.com/dev4.silvertech.net/products/reflectance-materials-and-coatings/high-reflectance-materials/optical.aspx> (2012).
22. V. V. Tuchin, *Tissue Optics: Light Scattering Methods and Instruments for Medical Diagnosis* (SPIE Press, 2007).
23. R. Marchesini, A. Bertoni, S. Andreola, E. Melloni, and A. E. Sichirollo, "Extinction and absorption coefficients and scattering phase functions of human tissues in vitro," *Appl. Opt.* **28**(12), 2318–2324 (1989).

1. Introduction

There is a near complete lack of imaging used to visualize tumor involvement at the margins during breast conserving surgery, and this is believed to be a major reason for the fact that the majority of women are recalled for additional surgeries. Optical techniques based on absorption, fluorescence or other in-elastic light scattering rely on bio-chemical contrast mechanisms to distinguish tumors from normal tissue, and often require the use of an exogenous contrast agent for imaging. Tissue morphology presents a reliable endogenous contrast mechanism to distinguish breast pathologies, and offers a 'label-free' approach to margin assessment if a sensitive imaging technique could be developed to exploit this contrast. In optical imaging, spectral, angular and polarization dependence of elastic light scattering provide a comprehensive suite of morphology-sensitive signals that could be used to image this intrinsic contrast. In this study, a unique localized spectroscopy system was developed to provide a platform from which quantitative spectroscopy of surgical tissues could be completed in an imaging geometry.

Conventional full-field imaging via surgical microscopes coupled to CCD cameras are routinely used in OR settings, and could be easily adapted to perform spectral imaging of resected specimens. However this technology is not able to image morphological contrast at

sufficiently high resolutions because of the overwhelming diffuse background arising from the sub-surface tissue structures. In addition, wavelength dependent absorption due to tissue chromophores such as hemoglobin and lipids create a non-specific contrast that is difficult to decouple from the scattering signal.

Localized spectroscopy allows high-resolution sampling of the scatter contrast by effectively suppressing the diffuse background caused by strong multiple scattering in tissue [1, 2]. Signal localization in these geometries restrict light transport to approximately a few hundred microns in depth, offering inherent insensitivity to changes in background absorption allowing direct sampling of the scatter signal that has not passed through much path-length in tissue [1]. In practice, this type of localized signal sampling is easily implemented using optical fiber based probes. In fact several optical fiber probes have been developed in the past to exploit one or more combinations of optical contrast mechanisms, and have shown significant potential to reliably delineate malignant from benign tissues [3–6]. However, probe-based techniques only offer limited sampling of tissue regions and hence do not adequately capture the high natural variability in local tissue scattering properties. In addition, co-registration of probe data with standard histopathology is not trivial at resolution scales relevant to surgical margin assessment.

Direct adaptations of probe-based approaches to imaging can involve mechanically scanning or positioning the probe head across the tissue surface, which is time consuming and does not scale well for efficient wide field imaging of large tissue specimens, that is needed for comprehensive margin assessment [7–11]. Similarly, scanning confocal approaches offer sufficient signal localization and imaging capabilities in a scalable, non-contact design that can help characterize tissue heterogeneity effectively. Particularly, recent developments have highlighted the potential of confocal imaging in detecting skin and oral lesions [12, 13]. But the conventional microscopic confocal systems [14] are optimized for high resolution, depth-sectioned imaging over narrow fields of view, which again is not suitable for imaging cancer margins across large fields. While mosaic imaging techniques could be used to extend the field of view [15, 16], these designs do not maintain a consistent sampling geometry at each pixel position, which makes it particularly unsuitable for imaging tissue scatter signals that are known to exhibit spatial and angular dependence [17].

A quantitative, noncontact scanning spectroscopic imaging system was developed to address these issues and allow better characterization of breast tissue specimens for margin assessment applications. The system uses a novel telecentric scanning approach to combine dark-field and confocal imaging principles to allow direct imaging of the localized scatter contrast in bulk tissue specimens. The telecentric architecture ensures consistent sampling geometry throughout the entire imaging field and the dark-field configuration rejects the specular reflections arising from the tissue interface, which could lead to reduction in the scatter contrast. In this work the imaging system was validated for breast tissue specimen imaging.

2. Materials and methods

2.1 Scanning *in situ* Spectroscopy (SiS) imaging platform design

A Scanning *in situ* Spectroscopy imaging platform was developed to allow localized spectroscopic imaging of 1 cm x 1cm large thick tissue specimens. The design employs a novel dark-field illumination and localized detection scheme to raster scan tissue surfaces for dense spectral sampling at each pixel. A five-element apochromatic, telecentric scan lens was custom designed to maintain a consistent sampling geometry and spot size across the entire imaging field, and over the designed waveband (400-700 nm). A schematic of the system is presented in Fig. 1 and the design details are highlighted in [18] and reproduced here for clarity. In the illumination path, broadband light from a supercontinuum light source (SCL, Koheras AG, Denmark) is fiber-coupled into a 200 μ m core diameter multimode optical fiber (IF) through a collimation-refocus assembly (FC), and is wound tightly around a vibrating assembly (CS) to minimize speckle noise. Compared to the system in [14] that used a 50 μ m

core diameter fiber, coupling the supercontinuum output to a larger 200 μm core diameter fiber through FC and CS allowed reduction of speckle noise, but also resulted in a slightly larger spot size at the sample plane. Light from the distal end of the multimode fiber is collimated back using a custom fabricated optical assembly (L1) consisting of an achromatic lens bonded to a 45° micro-rod mirror. L1 produces a hollow collimated beam of light with an outer diameter of 10 mm and inner diameter of 6 mm, suitable for dark-field illumination, which is scanned by a two-axis galvanometric scanning system (GS) positioned at the entrance pupil of a custom designed telecentric scan lens (TCL). The telecentric design allows normal illumination of the sample at all field positions, ensuring a consistent sampling geometry across the entire sample. A manual micrometer-controlled, two-axis linear translation stage (SAM), with a removable glass slide assembly, is used to hold each sample. It is mounted such that the top surface of the glass slide is located at the best focus plane of TCL.

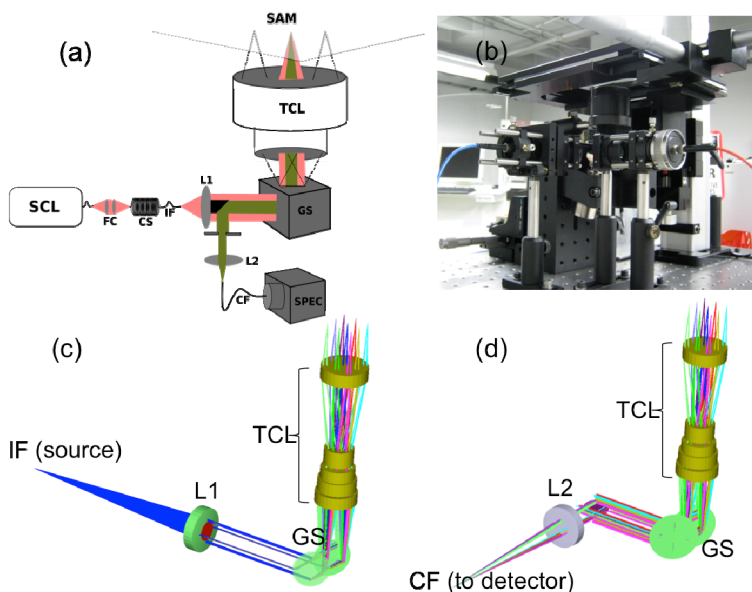


Fig. 1. (a) A schematic of the dark-field Scanning *in situ* Spectroscopy (SiS) imaging platform (b) a photograph of the SiS platform (c) ZEMAX optical layout of the illumination optical path (d) ZEMAX optical layout of the detection optical path.

In the detection path, the reflected (specular) and scattered light from the glass-tissue interface is re-collimated by the TCL, de-scanned by the scanning mirrors, and directed back towards L1. In an ideal telecentric and dark-field illumination geometry, all light specularly reflected into the detection path would pass through L1 without entering the detection arm and scattered light would be collected in the hollow region for direction into the detection arm by the mirror portion of L1. However, in the presence of aberrations and slight alignment inconsistencies, a portion of the reflected light also enters into the detection arm around the periphery of the detection aperture and is blocked using an aperture stop (AS). Another achromatic lens (L2) is used to focus the light scattered back from the specimen on the face of a 50 micron core diameter optical fiber coupled to a thermoelectrically cooled CCD-based imaging spectrometer (SPEC). SiS images are generated by raster scanning the illumination spot across the specimen and recording the localized spectral remission at each pixel position. In this work, the SiS imaging platform was characterized for imaging localized scattering properties of lumpectomy surgical specimens.

2.2 ZEMAX modeling and analysis

The entire illumination optics train, including the scan mirrors, was modeled in ZEMAX to optimize the design and to evaluate the overall performance of the imaging optics. Figure 1(c) shows the ZEMAX layout of the illumination train from the source fiber to the sample plane. The telecentric lens TCL used in this design was custom designed in collaboration with Special Optics Inc., NJ. An iterative design approach was used to balance the aberrations in the entire optical system to achieve a uniform target spot size at all scan field positions and across the entire design waveband of 400-700 nm. The dark-field scanning design required excellent telecentricity performance over the entire field, which was the other major design focus.

The multi-configuration layout capability of ZEMAX was used to create individual ray traces for nine scan field positions, covering the center and the extreme positions of an 1 cm x 1 cm scan field as shown in Fig. 2(a). Each configuration corresponds to a specific set of deflection angles for the scan mirrors, which 'scanned' the focused spot at the sample plane to one of the nine locations considered. The fiber face was modeled as a 200 μ m diameter circular disc with uniform illumination, which is a more accurate representation of the source compared to the earlier approach of using a collection of point sources to model the fiber output as outlined in [18].

Further analysis of the optical design revealed that the loss of telecentricity at extreme field positions was mainly due to the separation of the X and Y scanning mirrors, which can cause a scan angle-dependent pupil shift in the transverse plane. The entrance pupil of the TCL is often placed midway between the two scan mirrors along the optical axis to minimize the effects of this pupil shift. However, in the presence of other aberrations in the optical system, this conventional placement does not always guarantee the best performance. This effect was analyzed using ZEMAX; the detection train was modeled by folding the optical path at the sample plane by placing a virtual mirror and tracing specularly reflected rays back through the illumination optics to the detection fiber. The ZEMAX layout for the detection path is shown in Fig. 1(d). The conventional placement of the entrance pupil of TCL at the midway position between the two scan mirrors was tested using this model and found to produce poor telecentricity performance, not optimizing geometric separation of the specularly reflected and scattered light in the detection path. However, shifting the location of the entrance pupil away from the midway position and towards the second scanning mirror resulted in an optimal placement that minimized this coupling in the detection path. This optimal location was used as a starting point in the system fabrication/alignment process and fine-tuned to balance telecentricity performance across the entire field.

2.3 Spot size calculations and measurements

Complete modeling of the optical system in ZEMAX also allowed theoretical calculation of the illumination spot size at the center and at eight positions uniformly distributed within the 1 cm x 1 cm field. Modeling the fiber face as a circular disc enabled the use of extended geometric image analysis feature in ZEMAX to calculate the 'image' of the source at the focal plane of the TCL for each of the nine positions evaluated here. This analysis accounts for all aberrations in the optical system and presents a realistic estimate of the focus spot size and its variations over the entire field. The analysis was also done at five discrete and uniformly spaced wavelengths spanning the 500-700 nm waveband to assess wavelength dependence of the spot size.

The spot sizes at the center of the field and one of the four extreme corners were also experimentally measured using the standard knife-edge technique [19]. Full spectral measurements were made at each position, which allowed calculation of the spot size at the same discrete wavelengths sampled in ZEMAX for comparison.

2.4 Signal stability and repeatability measurements

Each 1cm x 1cm acquisition requires approximately 12 minutes, so random temporal variations in the laser source power could affect scan uniformity. The temporal stability of the detected signal was analyzed by acquiring spectra from a spectralon reference standard in a continuous manner. The source was allowed to stabilize initially for ~30 minutes and two sequential data sets were acquired in 15-minute durations to assess source stability within a full field scan and across multiple sequential scans. This entire measurement sequence was repeated on another day to assess repeatability.

2.5 Intralipid and blood phantom measurements

The localized sampling geometry implemented here is inherently insensitive to changes in local absorption, thereby allowing for nearly direct measurement of scatter features. An array of tissue simulating phantoms, consisting of serially diluted blood in increasing concentrations of Intralipid, were imaged to assess the ability of the system to quantify scatter changes despite variations in background absorption. The volume fraction of Intralipid scatterers in the array of phantoms varied from 0.5% to 4%. The total hemoglobin concentration was serially diluted from 60 μ M to 3.8 μ M using heparinized porcine blood for all scattering concentrations. The blood hematocrit level was measured to allow calculating the actual hemoglobin concentrations. This array of phantoms adequately spans the range of scattering and absorption coefficients relevant to breast tissue, where the typical hemoglobin concentration ranges from approximately 10 to 40 μ M [20]. Measurements were made in glass bottom, 24-well plates (MatTe Corporation, Ashland, MA). A 5% Intralipid solution was used as the reference in all measurements to account for day-to-day variability in source strength and each phantom was thoroughly stirred before measurement to avoid settling issues.

2.6 Lumpectomy specimen imaging

Four resected breast tissues, each corresponding to a distinct and clinically relevant diagnosis, were acquired from breast conserving surgeries. The Dartmouth Institutional Review Board (IRB) approved the tissue procurement and imaging protocol. The tissue sections were imaged in an inverted geometry, through a glass plate mounted on the sample holder. The four corners of the 1 cm x 1 cm imaging field were marked using pins coated with India ink and the sample was immediately sent to pathology for routine histology processing; images were co-registered with the most superficial histology section using the holes left by the pins and the inked markings. The tissue sections were carefully chosen to represent different breast pathologies including, normal pathology (NOR), fibrocystic disease (FCD), invasive breast carcinoma (INV) and Ductal Carcinoma In Situ (DCIS). The imaging time for each sample was ~12 minutes. All specimens were rinsed in Phosphate Buffered Saline to remove free blood from the imaging surface and to keep the samples hydrated during imaging.

2.7 Spectral parameterization

The measured spectra at each pixel position were background subtracted and normalized relative to measurements from a gray Spectralon standard (SRS-05, LabSphere Inc., NH, nominal albedo = 0.05). The albedo of this gray spectralon standard is comparable to that of the measured surgical breast tissue specimens, allowing same acquisition settings to be used for both the sample and reference scans. The normalized spectral reflectance (R) data were then fit to the well-known power law type empirical model of reflectance, $R(\lambda) = A(\lambda)^{-b}$, to extract the relative scatter power (b) and scatter amplitude (A) parameters. Integrated reflectance was also estimated in the 610nm-700nm waveband that avoids the major hemoglobin absorption peaks [1, 18].

3. Results

3.1 ZEMAX spot profile calculations and experimental measurements

Figure 2(a) shows the theoretical polychromatic spot diagram at the imaging plane, at the center and eight extreme positions of the 1 cm x 1 cm imaging field. Figures 2(b-c) show line plots across the diameter of focus spots at the center and one of the corner positions of the full field. The line plots are shown at five discrete wavelengths within the 500-700 nm waveband. Figure 2(c-d) shows the experimentally determined spot size profile measured using the standard knife-edge technique. Though full spectral measurements of these line profiles were obtained, only the data at discrete wavelengths considered in Fig. 2(b-c) are shown here to allow direct comparison with the theoretical spot sizes.

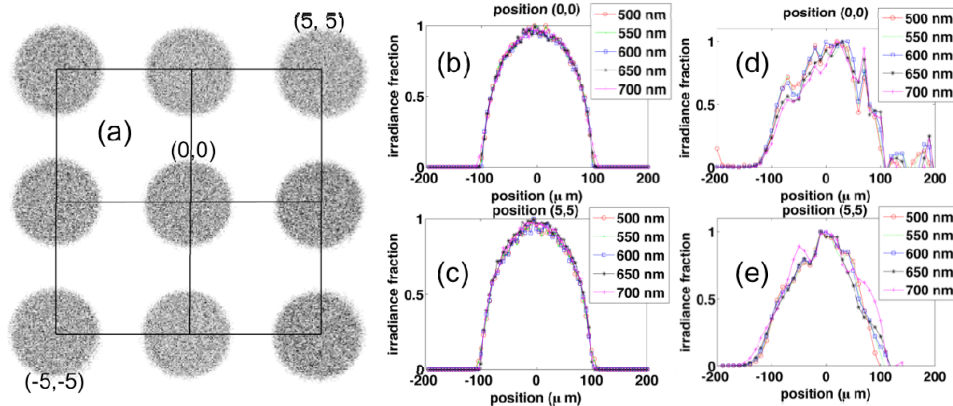


Fig. 2. (a) Focus spot profiles at the sample plane shown at 9 different field positions including the center and the extreme field positions (co-ordinates shown are in millimeters). The spots are shown enlarged to illustrate size uniformity and shape symmetry expected in a telecentric design (b-c) the theoretical estimates of spot size at the center (0,0) and an extreme (5,5) field positions. (d-e) experimentally measured spot size at the same field positions

3.2 System characterization and phantom measurements

Figures 3(a) and 3(b) show the average reflectance image and its histogram for a Spectralon sample measured over the 1 cm² field. A small fraction of pixels in the imaging field are shown masked due to signal artifacts caused by dust imperfections on the slide that resulted in spurious background data and hardware issues resulting in inconsistent data transfer from the spectrometer's CCD buffer. Figure 3(c) shows the relative standard deviation spectra for two sequential 15-minute continuous measurements made at a single field position. To assess long-term repeatability the same measurements were repeated on a different day and the results are shown in Fig. 3(d).

Figure 3(e) shows the average scattering spectra acquired from all Intralipid-blood measurements relative to the 5% Intralipid solution. Figure 3(f) shows a linear relationship between reflectance integrated in the 610-700 nm waveband and the Intralipid concentration. Figures 3(g-h) show the plots of the relative scatter amplitude (A) and relative scatter power (b) as a function of Intralipid concentration, assuming a power-law dependence on scattering. The mean and standard deviations of each scattering parameter as a function of hemoglobin variation are plotted in Fig. 3(f-h).

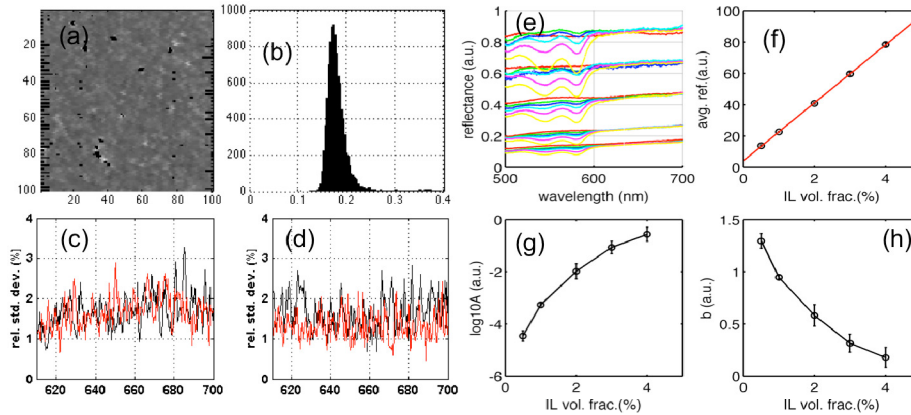


Fig. 3. (a) Average reflectance image of a spectralon standard (b) histogram of the average reflectance image showing no banding effects or patterns. Coefficient of variation is about 0.1 (c) Relative standard deviation spectra of two sequential, 15-minute, single spot measurement sequences. (d) Results from repeating the same set of measurements in (c) on a different day. (e) Reflectance spectra from a matrix of intralipid-blood phantoms, each group represents data from one particular intralipid concentration. Background hemoglobin concentrations for each group varied from 0 to 60 μM . Only the spectral waveband from 610 to 700nm was used to extract the scatter parameters. (f-h) Plots of average reflectance, logarithm of relative scatter amplitude and relative scatter power respectively, as a function of intralipid concentration. Error bars show variations in estimates due to change in background hemoglobin concentration.

3.4 Lumpectomy specimens imaging

Figure 4(a-d) shows images of the integrated reflectance and the relative scatter power from four pathologically distinct breast tissues, imaged within a 1 cm x 1 cm field of view. Each row shows a photograph of the tissue, a superficial histology section co-registered with the imaged surface and corresponding maps of the relative scatter power and integrated reflectance. Box and whisker plots of the scatter parameters are plotted in Fig. 4(e) and 4(f) to show the heterogeneity observed within a given tissue type.

4. Discussion

A dark-field telecentric scanning spectroscopy platform was characterized for direct imaging of local scatter parameters in surgically excised breast tissues. The inverted imaging geometry allowed the breast specimens to conform to the surface of the glass plate to provide a flat specimen required for confocal sampling. ZEMAX modeling of the entire optical train was used to theoretically estimate the illumination spot size, which was $\sim 168\mu\text{m}$ in the visible waveband explored here. The spot size was also verified experimentally using the standard knife-edge technique and was found to be $\sim 154\mu\text{m}$, matching the theoretical prediction well. Both theoretical and experimental spot profiles demonstrated excellent color correction and spot size uniformity across the 1cm x 1cm imaging field and within the design waveband, as expected in a telecentric design. Though the scan lens used here can support an imaging field of up to 2 cm x 2 cm, the effective field size was reduced because the transverse pupil shift caused by the spatially separated 2-axis galvanometric scanning system limited telecentricity at the extreme field positions. This slight loss of telecentricity resulted in a significant portion of specular light coupling into the detection path, thereby preventing accurate measurements of scattered light.

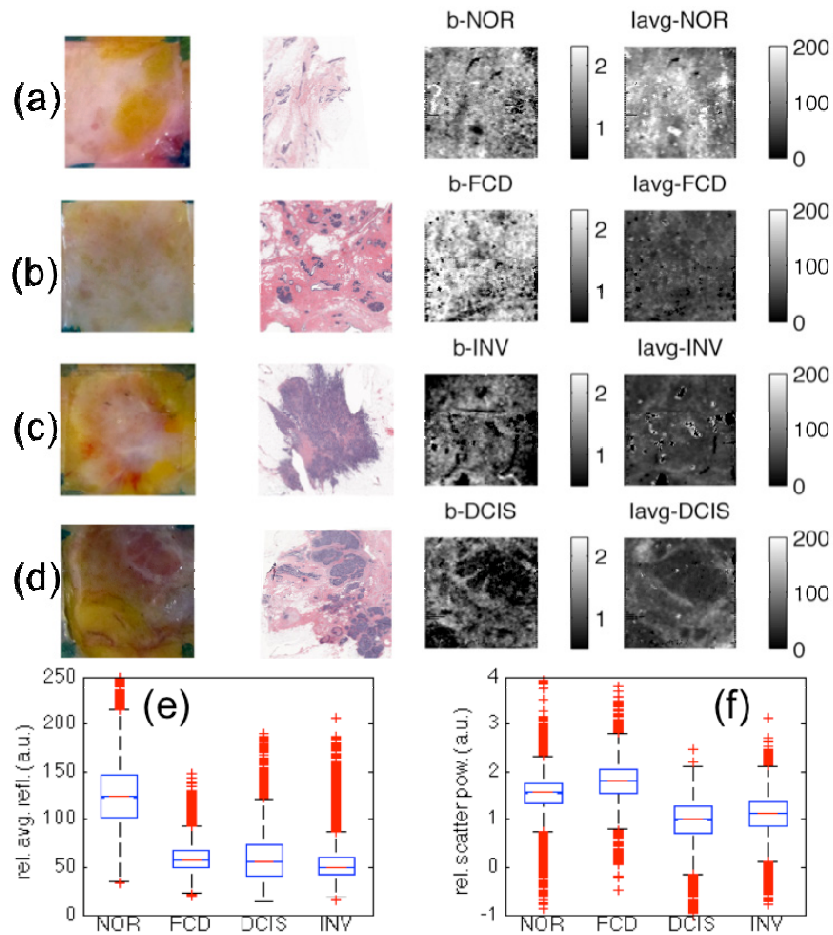


Fig. 4. Lumpectomy specimen images and scatter parameters trends for (a) normal (NOR); (b) fibrocystic disease (FCD); (c) ductal carcinoma in situ (DCIS), and (d) invasive carcinoma (INV). The scatter parameters scatter power (b) and integrated reflectance (lavg) are shown at right, with the white light and H&E shown left. The relative reflectance for each is shown in (e) and the relative scatter power, b, shown in (f).

The homogeneity of the imaging field was tested by scanning 1cm x 1cm of a Spectralon standard. The integrated reflectance shown in Fig. 3(a) showed no significant gradients or patterns indicating the absence of any field dependent aberrations in the optical system. Small-scale random variations observed are likely caused by the minute surface profile changes, which occur on length scales of 3-265 μ m [21]. The signal was stable temporally, as evaluated over multiple scan periods and on different days, with an average relative standard deviation of \sim 1.5%.

Measurements from liquid, tissue simulating phantoms, demonstrate insensitivity of the measured scattering signal to changes in absorption over the 610 – 700nm waveband; indicating that this localized sampling geometry may be used for direct scatter imaging. Scatter spectra were analyzed according to an empirical approximation to Mie scattering, which assumes a power law dependence on spectral light scattering. It should be noted that the spectra measured here are influenced by changes in both the scattering coefficient and the phase function. While it is possible to measure these effects independently by acquiring reflectance measurements at multiple angles [22, 23], the current design integrates the

scattering spectra across the illumination spot and so only the combined information can be measured.

Finally, scattering images from four distinct, and clinically relevant breast tissue types indicate significant variations in the scatter features within a given pathology, as high as 60% in some cases. This level of variation is consistent with data obtained from the first generation scatter spectroscopy system described here [1]. High-resolution sampling here was enabled by a dark-field design to allow quantitative characterization of this natural, spatial variation in scattering from local tissue morphology, which is not feasible using probe-based sampling and traditional imaging approaches. The preliminary results appear to indicate discernible contrast between benign (NOR/FCD) and malignant groups (INV/DCIS) despite the high natural variation observed within these pathologies. But delineating INV from DCIS would likely be challenging because of the subtle contrast in the relative scatter response. Preserving the spatial context thorough imaging allows investigating new contrast mechanisms including texture and shape features that could be computed on different size scales, which could improve delineation of pathologies in these cases where the local scatter response alone may not sufficient. More clinical studies are required to test the performance of this imaging technique relative to standard histopathology analysis.

5. Conclusion

A non-contact localized spectroscopic imaging platform was developed and validated for imaging breast lumpectomy tissue specimens. The entire optical system was modeled in ZEMAX for optimization and analysis of system performance. Both theoretical and experimental analysis of system performance indicated excellent color correction and aberrations control in the optical system that yielded uniform illumination spot sizes across the imaging field and designed waveband. Measurements from Intralipid-blood phantoms demonstrate the ability of the system to directly image local scatter parameters, independent of absorption changes in the range typically observed in breast tissue. Preliminary images of scattering from lumpectomy tissues showed significant variations in the local scattering response within a given pathology; characterization of this variance within tissue-types is critical to improving the performance of tissue classification algorithms. Finally, the modular nature of this platform facilitates adaptations that support different imaging modalities and optimizing imaging parameters like spot size, numerical aperture etc., which could be used to optimize contrast sensitivity of the current design and to investigate complementary contrast mechanisms in future studies.

Acknowledgments

This work was supported by funding from the NIH/NCI grant number PO1CA80139 and the Department of Defense Predoctoral Traineeship Award number BC093811.